Editors' Suggestion

Magnetic and electronic ordering phenomena in the Ru_2O_6-layer honeycomb lattice compound $AgRuO_3$

Walter Schnelle,* Beluvalli E. Prasad,† Claudia Felser, and Martin Jansen
Max Planck Institute for Chemical Physics of Solids, 01187 Dresden, Germany

Evgenia V. Komleva and Sergey V. Streltsov
Mikhail Nikolaevich Mikheev Institute of Metal Physics, Ural Branch of the Russian Academy of Sciences, 620137 Ekaterinburg, Russia and Ural Federal University, Mira Street 19, 620002 Ekaterinburg, Russia

Igor I. Mazin
Department of Physics and Astronomy and Quantum Science and Engineering Center, George Mason University, 22030 Fairfax, Virginia, USA

Dmitry Khalyavin and Pascal Manuel
ISIS Neutron and Muon Source, Rutherford Appleton Laboratory, Didcot OX11 0QX, United Kingdom

Sukanya Pal, D. V. S. Muthu, and A. K. Sood
Department of Physics, Indian Institute of Science, Bangalore 560012, India

Ekaterina S. Klyushina and Bella Lake
Helmholtz Zentrum Berlin für Materialien und Energie, 14109 Berlin, Germany and Institut für Festkörperphysik, Technische Universität Berlin, 10623 Berlin, Germany

Jean-Christophe Orain and Hubertus Luetkens
Laboratory for Muon-Spin Spectroscopy, Paul Scherrer Institute, 5232 Villigen PSI, Switzerland

(Received 8 March 2021; accepted 17 May 2021; published 4 June 2021)

The silver ruthenium oxide $AgRuO_3$ consists of honeycomb $Ru_2^{5+}O_6^{2-}$ layers and can be considered an analogue of $SrRu_2O_6$ with a different intercalation. We present measurements of magnetic susceptibility and specific heat on $AgRuO_3$ single crystals, which reveal a sharp antiferromagnetic transition at 342(3) K. The electrical transport in single crystals of $AgRuO_3$ is determined by a combination of activated conduction over an intrinsic semiconducting gap of ≈100 meV and carriers trapped and thermally released from defects. From powder neutron diffraction data a Néel-type antiferromagnetic structure with the Ru moments along the c axis is derived. Raman spectroscopy on $AgRuO_3$ single crystals and muon spin rotation spectroscopy on powder samples indicate a further weak phase transition or a crossover in the temperature range 125–200 K. The transition does not show up in the magnetic susceptibility, and its origin is argued to be related to defects but cannot be fully clarified. The experimental findings are complemented by density-functional-theory-based electronic structure calculations. It is found that the magnetism in $AgRuO_3$ is similar to that in $SrRu_2O_6$, however, with stronger intralayer and weaker interlayer magnetic exchange interactions.

DOI: 10.1103/PhysRevB.103.214413

I. INTRODUCTION

Ruthenium and its compounds feature impressively diverse chemical and physical phenomena. This is reflected, for instance, in the oxidation states accessible within the wide span from −2 to +8 and by particular electronic and magnetic ground states formed in molecular compounds, as well as in extended solids. This is especially relevant in condensed matter research, where ruthenium oxides and chlorides continue to attract prominent attention. Accessibility of different valence states of Ru results in a dramatic variability of physical properties even within the same structural motif. Indeed, honeycomb $Ru^{3+}L_3$ layers (L = ligand atom) form one of

*walter.schnelle@cpfs.mpg.de
†Department of Chemistry, RV Institute of Technology and Management, Bangalore, 560076, India.

the cleanest Kitaev systems known so far, with strong bond-dependent anisotropic exchange [1–3], $Ru^{4+}L_3$ dimerizes at low temperatures and forms a unique covalent bond liquid above 270 °C [4]. The $Ru^{5+}L_3$ compound $SrRu_2O_6$ was argued to feature unusual quasimolecular orbitals (QMOs), which determine the suppression of the magnetic moment and robust antiferromagnetic (AFM) coupling [5,6].

In different structural contexts, Ru^{4+} is noted for other unique physical phenomena. For example, RuO_2 dioxide was recently shown to be an example of a novel magnetic state of matter, an antiferromagnet without Kramers degeneracy, with unique physical ramifications [7]. It also generates a series of perovskite compounds ranging from $SrRuO_3$, $CaRuO_3$, and $BaRuO_3$, all bad metals, ferromagnetic or nearly ferromagnetic, with a strong effect of magnetic fluctuations on transport [8–10], to $Sr_3Ru_2O_7$, featuring one of the first experimentally observed magnetic quantum critical points, and Sr_2RuO_4, an enigmatic material for many years (but not any more) strongly believed to be a spin-triplet superconductor [11,12].

The recently synthesized $AgRuO_3$ [13] [space group $R\bar{3}c$, $a = 5.2261(6)$ Å, $c = 32.358(5)$ Å, $Z = 12$] featuring Ru^{5+} $4d^3$ ions comes close to the concept of a two-dimensional (2D) material [14], since it consists of stacked honeycomb Ru_2O_6 polyoxoanions, where the empty octahedral sites are capped on both sides with silver atoms. Thus the resulting $(Ag_2Ru_2O_6)_n$ slabs are charge neutral and resemble giant molecules. Based on magnetic susceptibility measurements on a powder sample, and a preliminary evaluation of time-of-flight (TOF) neutron diffraction data, it was claimed that $AgRuO_3$ showed strong magnetic exchange coupling. However, no long-range magnetic order could be detected at that time [13], while, in seeming contradiction with the experiment, first-principles calculations were predicting $AgRuO_3$ to be magnetically very similar to $SrRu_2O_6$ (supporting information for Ref. [12]). The latter has been investigated intensively—experimentally and theoretically—in the last years [5,15–24] and was shown to have the transition to a Néel-AFM ground state at $T_N \approx 560$ K. Recently, $BaRu_2O_6$ with the same crystal and magnetic structure and $T_N = 525$ K could also be synthesized [25,26].

Here, we present detailed measurements of the magnetic susceptibility, electrical resistivity, specific heat, and Raman spectroscopy on $AgRuO_3$ single crystals, as well as high-resolution TOF neutron data and muon spin rotation (μSR) data on polycrystalline material, all clearly demonstrating the presence of long-range AFM order up to ≈342(3) K. This relatively high Néel temperature of $AgRuO_3$ is in agreement with our first-principles analysis of the electronic structure. In several respects, $AgRuO_3$ parallels $SrRu_2O_6$; however, there are conspicuous differences. Specifically, there is a change in behavior, possibly a second phase transition, around 125–200 K within the AFM phase. It does not show up in either magnetic susceptibility or specific heat, but there are clear changes in both μSR and Raman spectra in this temperature range, and, in roughly the same range, the resistance shows nontrivial and nonmonotonic temperature behavior which can be explained by defect states.

In this paper we first present the extensive experimental findings, then complement these results with the electronic structure calculations, and finally sum up relevant implications. While the Néel transition at 342 K can be well described in terms of quasi-2D magnetic interactions resulting from the first-principles calculation and QMOs, the nature of the low-temperature phase transition(s) or crossover may be related to the defect states but remains not fully clarified.

II. EXPERIMENTAL AND CALCULATION DETAILS

For the measurements of various physical properties we used either portions of, or selected sets of tiny single crystals from the large polycrystalline sample of $AgRuO_3$ that had been synthesized as previously described [13].

Magnetization was measured on a set of ten selected single crystals (total mass 622 μg) with a MPMS3 (SQUID-VSM, Quantum Design) magnetometer. The crystals were glued with a minute amount of GE varnish to a quartz sample holder with the c axes oriented either parallel or perpendicular to the applied field. Prior to each measurement cycle, the sample was warmed to $T = 400$ K in zero field and then cooled to 2 K. Then the zero-field-cooled (ZFC) data were recorded in warming and the field-cooled (FC) data in cooling in different fixed magnetic fields, in a sequence of increasing target fields.

Electrical resistance was measured on several crystals by the four-probe ac method [RES option, Physical Property Measurement System 9 (PPMS9), Quantum Design]. Contacts in the hexagonal a plane of the crystals ($I \perp c$) or at the bases of short prismatic crystals ($I \parallel c$) were made with Pt wires (25 μm) and silver paint. The geometry factors could not be determined reliably (for resistivity data on a polycrystalline sample, see Fig. 2 of Ref. [13]).

Heat capacity up to 300 K was measured on a cold-pressed pellet with the HC option of a PPMS9 (Quantum Design) in magnetic fields up to $\mu_0 H = 9$ T. Above 300 K the melting of the thermal contact agent (high-vacuum grease Apiezon N) led to unreliable results. Therefore additional heat capacity data were obtained with a differential scanning calorimeter (DSC; PerkinElmer DSC8500) at heating rates of 5 and 20 K/min.

Neutron diffraction measurements were performed at the ISIS pulsed neutron and muon facility of the Rutherford Appleton Laboratory (UK), on the high-resolution cold-neutron diffractometer WISH located at the second target station [27]. Polycrystalline $AgRuO_3$ (≈2 g) was loaded into a cylindrical 6-mm-diameter vanadium can and measured on warming using an Oxford Instruments cryostat and a closed-cycle refrigerator (CCR) with a hot stage, respectively. Rietveld refinement of the crystal structure was performed using the FULLPROF program [28] against the data collected in detector banks at average 2θ values of 58°, 90°, 122°, and 154°, each covering 32° of the scattering plane.

Temperature-dependent Raman spectroscopy experiments were carried out on crystals using a Linkam THMS350V in the range of 77–385 K. The sample was cooled with a continuous flow of liquid nitrogen. Raman spectra were recorded in a LabRam spectrometer (Horiba) in backscattering geometry, using a ×50 objective and laser excitation of 532 and 660 nm.

Zero-field (ZF) μ^+SR (μSR) measurements of polycrystalline $AgRuO_3$ were performed using the Multi Purpose Surface-Muon Instrument (Dolly) and General Purpose

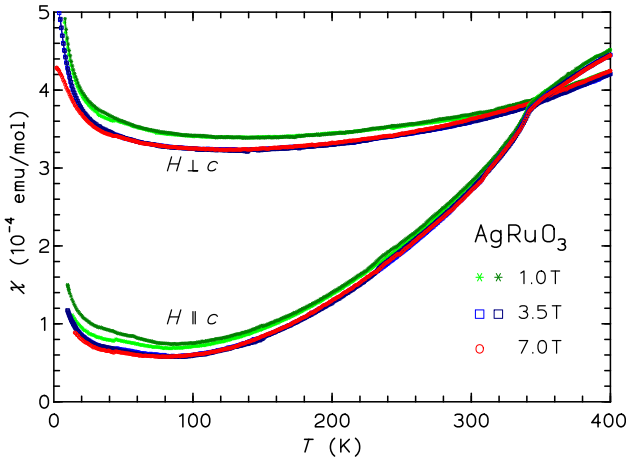

FIG. 1. Magnetic susceptibility $\chi(T)$ of $AgRuO_3$ crystals measured in different fields parallel and perpendicular to the crystallographic c axes. For 1.0 and 3.5 T the lighter and darker color symbols indicate measurements with the ZFC and FC protocol, respectively (see text). The ZFC and FC data almost coincide, except for the lowest temperatures. Large portions of the 3.5-T curves are obscured by the 7.0-T curves.

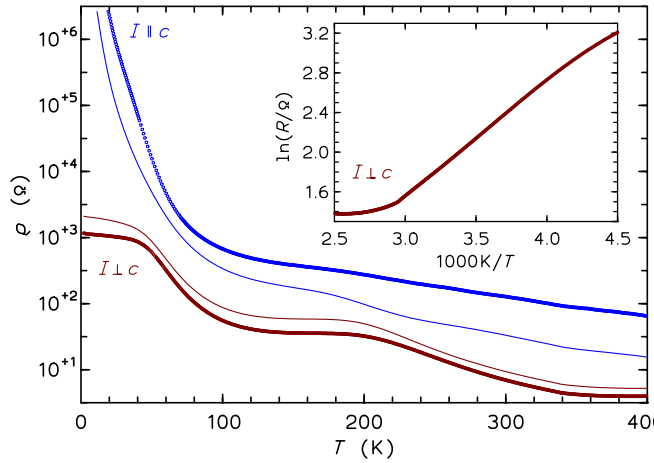

FIG. 2. Electrical resistance $R(T)$ of selected $AgRuO_3$ crystals for the current in the hexagonal a plane ($I \perp c$), or along the c axis ($I \parallel c$). The inset shows the Arrhenius-type plot of the in-plane resistance data. The thick and thin curves represent the data for two typical samples.

Surface-Muon Instrument (GPS) muon spectrometers at the Swiss Muon Source. For the measurements, 1.8 g of powder $AgRuO_3$ were pressed into a pellet and mounted on a silver sample holder. The measurements were performed over the temperature ranges 0.2 K $< T <$ 65 K using an Oxford Heliox and 65 K $< T <$ 295 K in an Oxford Variox cryostat.

The crystal structure for the electronic structure calculations was taken from Ref. [13]. The band structure calculations were performed using WIEN2K [nonmagnetic generalized gradient approximation (GGA)], including Wannier function projections [29], and the Vienna *ab initio* simulation package (VASP, all magnetic calculations) [30]. We utilized the projector augmented-wave (PAW) method [31] with the Perdew-Burke-Ernzerhof (PBE) GGA functional [32]. The energy cutoff chosen in VASP was $E_{\text{cutoff}} \sim 600$ eV and the $6 \times 6 \times 6$ Monkhorst-Pack grid of k points was used in the calculations.

III. RESULTS

A. Magnetism

The magnetic susceptibility of $AgRuO_3$ up to 400 K is shown in Fig. 1. Generally, the molar susceptibility is small. Above $T = 20$ K it is only weakly dependent on the applied field, and the ZFC and FC protocol data almost coincide. For $H \parallel c$ the susceptibility $\chi_\parallel$ displays a sharp kink at $T_N =$ 342 K, below which $\chi_\parallel$ strongly decreases. $\chi_\perp(T)$ shows a weak temperature dependence and a very weak kink at the same temperature (the slope is larger above T_N). Interestingly, the values of $\chi_\parallel$ and $\chi_\perp$ coincide at T_N, but at $T = 90$ K the anisotropy $\chi_\perp/\chi_\parallel \approx 6$. These findings suggest an AFM order with the Ru moments aligned along the c axis. Up to our maximum field of 7 T the magnetization data show no indication for a spin-flop or other metamagnetic transition.

Well below the ordering temperature, $\chi(T)$ for both directions shows a weak upturn, which we attribute to Curie-paramagnetic impurities or charged defects in the sample. An estimate can be made by fitting the 1.0-T data for $H \parallel c$ from 10–100 K to the Curie law $C/T + \chi_0$. Here, C corresponds to 0.10 μ_B, equivalent to 0.3% of spin-1/2 magnetic species. It should be mentioned that in measurements on loose powder samples (cf. Fig. 3 in Ref. [13]), preferential alignment of the crystallites along the easy axis can occur at high applied fields (typically, $\mu_0 H \geqslant 1$ T). In measurements on powders in low applied fields, no phase transitions or indications for a weak ferromagnetic component of the AFM order were detected.

B. Electrical transport

The temperature dependence of the electrical resistance was measured on several single crystals. The characteristics of the resistance curves measured with the current in the a plane ($I \perp c$) are well reproduced on several crystals (Fig. 2, red curves). With decreasing temperature the resistance generally increases, and at $T_N \approx 340$ K a change to a steeper slope (activated conduction; cf. inset of Fig. 2) can be observed. A plateaulike behavior is seen between ≈190 and ≈130 K, below which the resistance starts to rise again. Finally, the in-plane resistance appears to reach another plateau below $T < 30$ K. This characteristic behavior is in stark contrast with the c-axis resistance (Fig. 2, blue curves), which is roughly an order of magnitude higher and increases continuously with decreasing temperature, seemingly indicating a different activated conduction behavior. At $T \approx 130$ K a changeover to a much stronger slope is observed. It has to be mentioned that not all crystals showed such high resistance at low T (compare the two blue curves in Fig. 2), which might be due to poor mechanical quality of the specimens. For all crystals a weak kink is visible in the a-plane resistance at the Néel temperature.

It is clear from the Arrhenius-type plot (Fig. 2 inset) that the charge transport in $AgRuO_3$ is largely due to activation processes. In order to get an idea of the involved

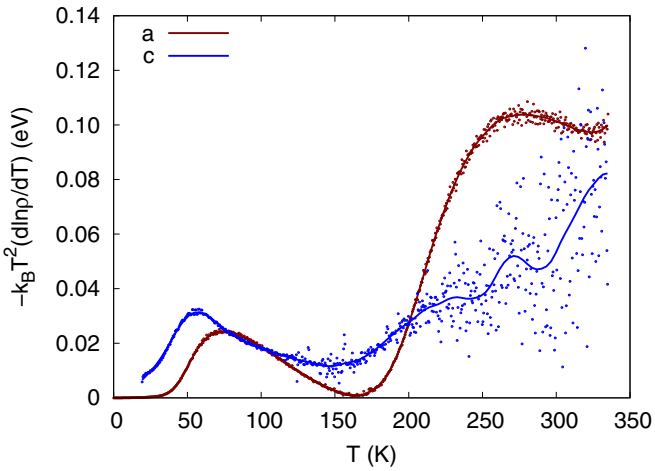

FIG. 3. Effective transport excitation gap defined as $E_g(T) = -k_BT^2(d\ln\rho/dT)$ for the current in the a plane or along the c axis. The solid curves represent spline-smoothed data.

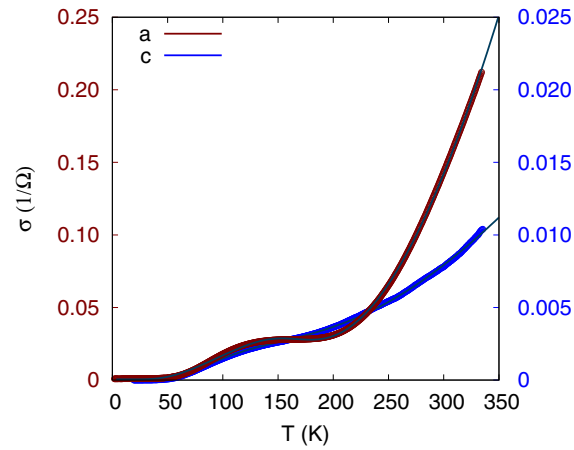

FIG. 4. Fitting to Eq. (2) (curves) of the experimental conductivity data (circles). The left (red) scale corresponds to the a plane; the right (blue) scale corresponds to the c-axis conductivity.

energy barriers, we have calculated the function $E_g(T) = -k_BT^2(d\ln\rho/dT)$ (Fig. 3). For both directions the activation barrier shows a profound temperature dependence, by no means attributable to a single gap. The high-T behavior is consistent with an activation gap of the order of 0.07–0.09 eV for both directions. The apparent gap drops nearly to zero around $T \sim 150$ K (170 K), for the c (a) directions, and increases again upon cooling to ∼55 K (75 K) to values of ∼0.035(0.025) eV, respectively. Then it drops to zero again as $T \to 0$.

While the temperature dependence of the derivative-deduced activation energy is qualitatively similar in both directions, the details are very different. Since the actual gap is a scalar quantity, the only way to reconcile this observation is to assume that there are several different reservoirs of charge carriers, one of them corresponding to the actual excitation gap, which should be larger than ∼0.1 eV, and the other(s) representing various defect states inside the gap. In the limit $T \to 0$, the conduction in the a plane appears to be governed by a merely constant conductivity σ_0 (of unknown origin and nature), while in the c direction the upper limit for our resistance setup is reached at 11 or 19 K, respectively, for the two data sets we show. In addition, there are defect states that contain a small number of carriers, and start to donate them at around 50 K but get depleted at higher temperature. A closer inspection shows that one also needs to introduce temperature-dependent scattering, presumably related to the same defect states and determined by a similar activation energy. Note that the defect-derived carriers dominate the low-T regime, while the high-temperature transport is affected by the carriers thermally excited across the fundamental gap. With this in mind, we tried to fit the conductivity $\sigma = 1/\rho$ with

$$\begin{aligned} \sigma &= n\tau, \\ n &= n_1\exp(-E_g/T) + \frac{n_2}{1+\exp(D/T)}, \\ 1/\tau &= 1/\tau_0 + \frac{1/\tau_1}{1+\exp(D'/T)}. \end{aligned} \tag{1}$$

As shown in Fig. 4, this provides a perfect fit to the data, although the parameters differ between the two directions. While the fit is not very sensitive to the parameters D and D', and they can be forced to be the same, with only moderate loss of the fit quality, the fundamental gap E_g is important for getting the high-temperature resistance right. We can only conclude that the transport in the c direction is contaminated by grain boundaries and other defects, or is plainly not Boltzmannian. The exceptionally large transport anisotropy is suggestive of that. The formula (simplified in the sense that all defect states are lumped together into a single parameter) is

$$\sigma = \frac{\sigma_0 + \sigma_1\exp(-E_g/T) + \sigma_2/[1+\exp(D/T)]}{1 + A/[1+\exp(D'/T)]}. \tag{2}$$

The parameters derived from the a-plane transport are $\sigma_0 = 5\times10^{-4}$, $\sigma_1 = 9\times10^3$, $\sigma_2 = 0.2\ \Omega^{-1}$, $E_g = 200$ meV, $D = 20$ meV, $D' = 115$ meV, $A = 1300$. As mentioned, D' can actually be set to be the same as D with only moderate deterioration of the fit. For the c axis the values are $\sigma_0 = 9\times10^{-8}$, $\sigma_1 = 2.1$, $\sigma_2 = 0.08\Omega^{-1}$, $E_g = 110$ meV, $D = 30$ meV, $D' = 30$ meV, $A = 20$. These fit parameters show strong interdependence and should not be taken as exact values.

One take-home message is that a defect level located at 20–30 meV (corresponding, roughly, to $T \sim 200$–300 K) is capable of generating the anomaly in the temperature dependence of transport, visually located at 150–170 K.

C. Specific heat

The specific heat is shown in Fig. 5(a) in a c_p/T vs T representation. In the covered temperature range, no peak or anomalous broadened feature can be seen, suggesting the absence of any phase transition. The data in the low temperature range [Fig. 5(b)] are well described by $c_p(T) = \gamma'T + \beta T^3 + \delta T^5$, with the latter two terms representing the phonon contribution. Fitting results in $\beta = 0.913(3)$ mJ mol^{-1} K^{-4}, corresponding to the initial Debye temperature of 220 K, and $\delta = -0.00060(1)$ mJ mol^{-1} K^{-6}, the next term in the harmonic lattice approximation constituting a small

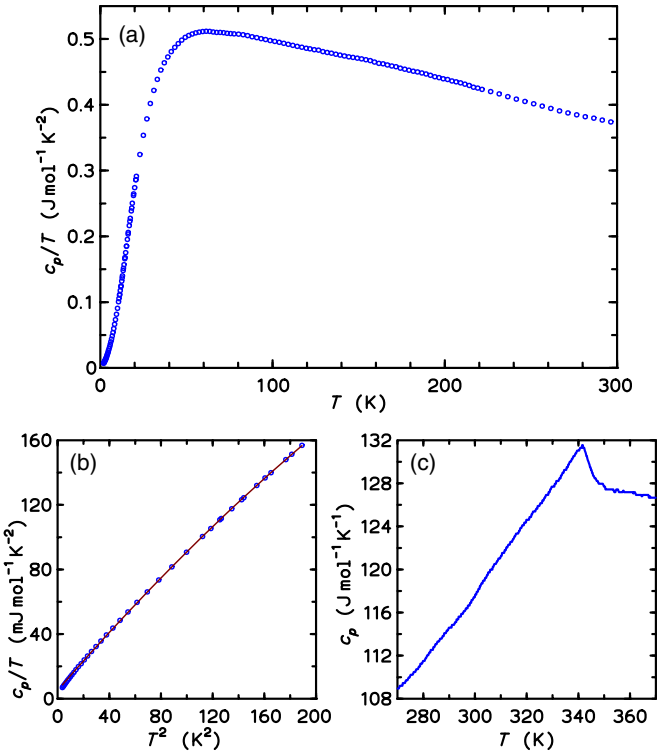

FIG. 5. (a) Specific heat of $AgRuO_3$. (b) Low-temperature data in the c_p/T vs T^2 representation. The curve is the fit as described in the text. (c) High-temperature differential scanning calorimetry (DSC) data; scan rate is 20 K/min.

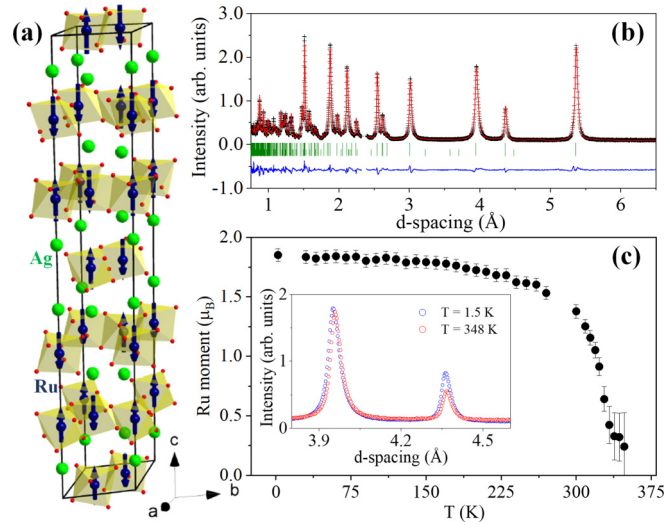

FIG. 6. (a) Schematic representation of the magnetic structure of $AgRuO_3$ with the $\bar{R}3'c'$ magnetic space group. (b) Rietveld refinement of the neutron diffraction pattern collected at $T = 1.5$ K ($R^{\text{Bragg}}_{\text{nuclear}} = 2.66\%$ and $R^{\text{Bragg}}_{\text{magnetic}} = 3.2\%$). (c) Ru ordered moment vs temperature. The inset shows two selected peaks for two different temperatures.

correction. The linear coefficient $\gamma' = 5.6(1)$ mJ mol^{-1} K^{-2} is quite large (there should be no conduction electron term). Similar linear terms have been observed previously [33], and they are probably due to a rather high concentration of point defects. It appears that the majority of these defects do not show up as an upturn of the magnetic susceptibility towards low T (cf. Fig. 1); thus they should be nonmagnetic, e.g., oxygen or silver defects. The changes in $c_p(T)$ with magnetic fields up to 9 T are very weak; thus we suppose that magnetic contributions are small in this temperature range far below T_N.

The DSC specific heat data [Fig. 5(c)] around room temperature are about 5% higher than the PPMS data and have realistic values close to the Dulong-Petit limit ($c_p \approx 3nR$, where $n = 5$ is the number of atoms and R is the gas constant). They display a clear second-order-type anomaly with the midpoint at $T_N \approx 344$ K, corroborating the long-range magnetic order at that temperature. No heating rate dependence of $c_p(T)$ or latent heat is observed. We assign this transition to the AFM long-range ordering of the Ru moments.

D. Neutron diffraction

To further confirm the presence of long-range magnetic ordering, we performed neutron diffraction measurements (1.5 K $< T <$ 348 K). The data revealed that some of the reflections demonstrate a strong temperature dependence below $T_N \approx 335$ K [Fig. 6(c), inset], which is consistent with the fact that the magnetic unit cell coincides with the cell of the nuclear structure and the subsequent refinement of the diffraction patterns [see, e.g., Fig. 6(b)] was done assuming zero magnetic propagation vector ($k = 0$).

The refinement was assisted by symmetry arguments based on the representation theory [34,35], and the parametrization for the magnetic form factor of Ru^{5+} was taken from Ref. [36]. We found that the simple magnetic structure with antiparallel alignment of spins on the nearest-neighbor Ru sites (Néel structure) provides a good refinement quality of the neutron diffraction data [Fig. 6(b)] in the whole temperature range below T_N. Surprisingly, the fit quality was found to be almost insensitive to the moment direction, complicating the choice between the models with in-plane and out-of-plane spin polarization. However, our density-functional-theory (DFT) calculations that take into account spin-orbit coupling (SOC; see Sec. III G for details) strongly support the model with the out-of-plane spin orientation, in agreement with the observed anisotropy of the magnetic susceptibility. Note that this spin direction was also found experimentally in another trigonal ruthenate, $SrRu_2O_6$ [16,24].

The magnetic structure of $AgRuO_3$ [Fig. 6(a)] implies $\bar{R}3'c'$ magnetic symmetry with the ordered moment size of 1.85(5) μ_B at $T = 1.5$ K. The moment varies smoothly with temperature [Fig. 6(c)] indicating that the anomalous behavior found between 170 and 225 K in the Raman and μSR measurements is likely to be predominantly nonmagnetic in origin.

E. Raman spectroscopy

Raman scattering has the ability to identify the role of phonons in structural and magnetic transitions, the latter via spin-phonon coupling. At ambient temperature, $AgRuO_3$ has a trigonal $R\bar{3}c$ structure with 25 Raman active modes of A_{1g} and E_g symmetries. Figure 7 shows the reduced Raman susceptibility $\chi''(\omega) = I(\omega)/[n(\omega) + 1]$, where $I(\omega)$ is the

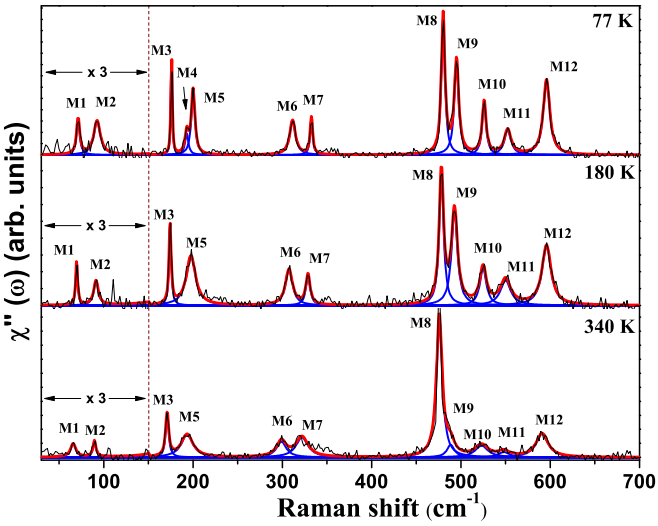

FIG. 7. Raman spectra of $AgRuO_3$ at typical temperatures (black curves). The solid red curve is a Lorentzian fit to the data; blue solid curves are individual fits of the Raman modes. The downward-pointing arrow in the top panel indicates the additional mode M4. The weak intensities below 150 cm^{-1} are magnified by a factor of 3.

observed intensity and $[n(\omega) + 1]$ is the Bose-Einstein factor, at a few typical temperatures. Lorentzian line shapes were fitted to $\chi''(\omega)$ to extract the phonon frequencies, full width at half maximum (FWHM), and integrated intensities of the Raman modes. Table S1 in the Supplemental Material [37] lists the experimentally (at 300 K) observed and calculated frequencies for the trigonal high-temperature AFM state, which are shown with the corresponding error bars in Fig. 8(b) and Fig. S1 of the Supplemental Material (for an explanation of how the error bars were decided for the theoretical values,

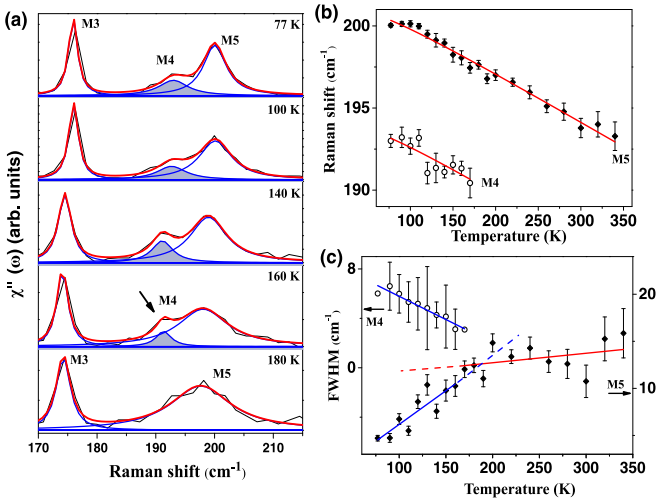

FIG. 8. (a) Temperature evolution of the Raman spectra in the range 170–215 cm^{-1}. The solid red curve is a Lorentzian fit to the data; blue solid curves are individual fits of the Raman modes. (b) Raman shift and (c) FWHM of the modes M4 and M5 plotted as a function of temperature. The red lines are fits to the anharmonic model, and blue lines are linear fits to the data.

see the Supplemental Material [37]). The agreement is nearly perfect. At 77 K, 12 first-order Raman modes (M1 to M12) are observed in the spectral range 30–650 cm^{-1}. Most noticeable is the disappearance of mode M4 above 170 K, while all other modes are present in our working temperature range.

To bring home this point clearly, Fig. 8(a) presents the fitted Raman spectra for selected temperatures in the spectral range 170–215 cm^{-1}. The temperature evolution of the frequencies and FWHM for modes M4 and M5 are shown in Figs. 8(b) and 8(c), respectively. The FWHM of mode M4 is anomalous; that is, it increases as the temperature is lowered. The FWHM of mode M5 also shows a significant change at 170 K. The temperature dependence of the frequencies and linewidths of the remaining phonons is given in the Supplemental Material, Figs. S1 and Fig. S2 [37], respectively. Phonon frequencies show the expected behavior of decreasing frequency as T is increased due to quasiharmonic (i.e., thermal expansion effect) and anharmonic effects [38]. The solid red lines in Figs. 8(b) and 8(c) are fits to the simple cubic anharmonic model where a phonon decays into two phonons of equal frequency [38], given by $\omega^{\text{cubic}}(T) = \omega(0) + C\{1 + 2n[\omega(0)/2]\}$, C being the self-energy parameter. Coming back to mode M4, it is clearly visible for both polarizations at $T = 77$ K (see Fig. S3 of the Supplemental Material [37]) but disappears at around 170 K. Figure 9(a) shows the integrated intensity of this mode as a function of T. Given the error bars, this dependence is equally well consistent with a linear behavior (shown), with an exponential decay in the entire temperature range, or a square-root dependence corresponding to a second-order phase transition at $T_c = 170$ K (both not shown).

As shown in Fig. 9(b), the intensity of mode M9 normalized with respect to mode M8 shows a distinct change at 170 K. The intensity of M9 gradually decreases with T and goes to zero near T_N. All these observations of distinct changes in temperature dependence of phonon modes M4, M5, and M9 indicate subtle structural changes around $T \approx 170$ K. However, the absence of any distinct features at this temperature in other probes suggests that these changes do not constitute a true phase transition, but indicate a crossover region stretching between 150 and 200 K. Note that this is the same range where the in-gap defect states strongly affect electrical transport, albeit a mechanism by which free carriers donated by these states can affect the Raman scattering is not clear.

We now come to the higher spectral range shown in Fig. 10(a), where we observe a weak broad band at 1155 cm^{-1}. To establish that this is a Raman mode and not photoluminescence, we did experiments at 77 K with two different incident photon excitations, 660 and 532 nm [shown with the thick green curve in Fig. 10(a)]. This confirms that the mode at ≈1155 cm^{-1} is a Raman mode. Figure 10(b) shows the temperature dependence of the integrated intensity of this broad band.

The T dependence of the frequency and the linewidth are shown in the insets of Fig. 10(b). In several Heisenberg antiferromagnets, such as in $YBa_2Cu_3O_6$ [39], Sr_2IrO_4, $Sr_3Ir_2O_7$ [40], and $SrRu_2O_6$ [21], two-magnon Raman modes have been observed in the magnetically ordered state. If the

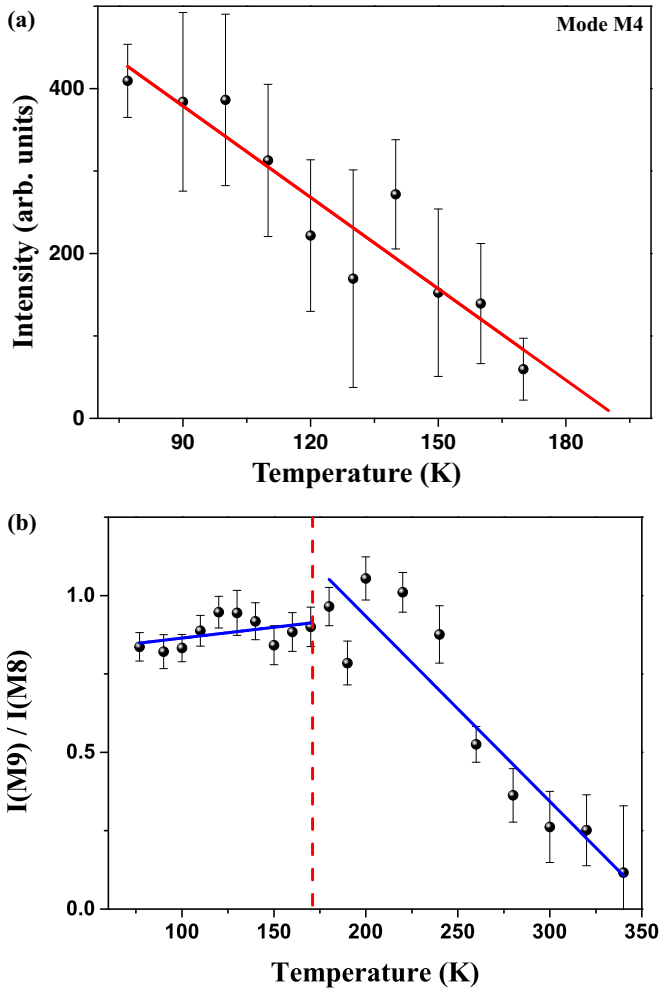

FIG. 9. (a) Temperature evolution of the integrated intensity of the M4 Raman mode. The red line is a linear fit resulting in an intercept $T_c = 193(5)$ K. (b) The ratio of integrated intensities of mode M9 to mode M8 shows a change in slope around 170 K. The blue solid lines are linear fits to the data below and above 170 K.

Heisenberg model is defined as

$$H = \sum_{i \neq j} J_{ij} \mathbf{S}_i \mathbf{S}_j, \tag{3}$$

then the frequency of two-magnon Raman scattering is $\sim 17J$ [21]. Taking $s = 1$, we get an estimate of $J \approx 97$ K, close to our calculated value (see Sec. III G below).

However, we cannot completely rule out the possibility of electronic Raman scattering associated with the electronic transition between the QMOs of Ru^{5+}, as in the case of $SrRu_2O_6$ [6], although, in principle, one would expect such transitions to manifest at higher energies.

F. Muon spin rotation spectroscopy

Figure 11(c) shows the time dependence of the muon spin polarization in $AgRuO_3$ measured in the Dolly spectrometer at the base temperature of $T = 0.2$ K in zero field (ZF). The modulated oscillations indicate the presence of an internal magnetic field in the sample due to long-range magnetic order.

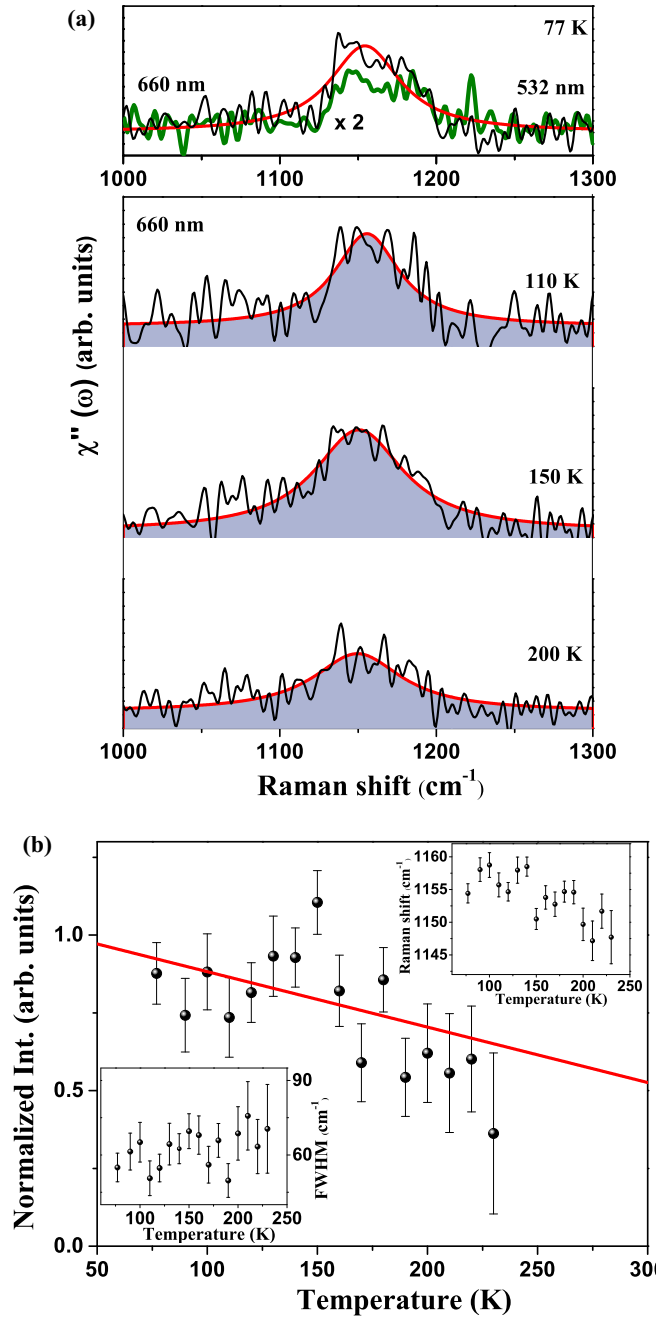

FIG. 10. (a) Top: The broad mode is observed with both 532-nm (shown by solid thick green curve) and 600-nm lasers at 77 K (raw data with the high-frequency noise filtered out). Bottom: Temperature evolution of the broad mode measured with the 660-nm red laser. The red curves are Lorentzian fits. (b) Temperature dependence of the intensity (Int.) of the broad mode. The red solid line is a linear fit to the data (guide to the eye). The frequency and the linewidth as a function of temperature are shown in the insets.

The fast Fourier transformation (FFt) of the data (Fig. 12) shows that, in general, there are two fractions of the muon spin ensemble, which oscillate with different frequencies giving rise to two peaks, ≈17 and ≈23 MHz. The presence of two frequencies can be attributed to two magnetically and/or crystallographically inequivalent muon stopping sites in the

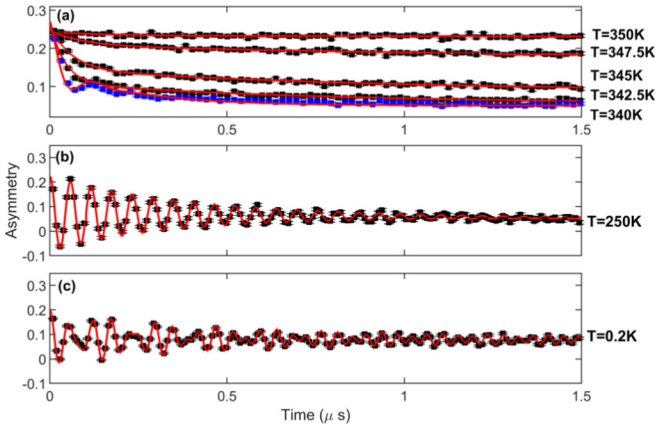

FIG. 11. Zero-field μSR spectra measured on powder $AgRuO_3$ at (a) $T = 342.5$, 345, 347.5, and 350 K using the GPS muon spectrometer; (b) $T = 250$ and (c) $T = 0.2$ K using the Dolly spectrometer. The red curves represent the best results of the fit analysis described in the text.

crystal structure. To extract the frequencies of the observed oscillations, the ZF-μSR spectrum at $T = 0.2$ K was analyzed with the software package MUSRFIT [41] using the fitting function

$$A(t) = \sum_{i=1}^{2} A_i \cos(2\pi \nu_i t) \exp(-\lambda_i t) + A_3 \exp(-\lambda_3 t). \quad (4)$$

Here, A_1 and A_2 are the amplitudes of the muon spin oscillations due to the component of the internal field which is perpendicular to the muon spin polarization; ν_1 and ν_2 are the frequencies of these oscillations which are connected to the internal field via the relation $\nu_i = \gamma_\mu |B_i|/2\pi$, where γ_μ is the muon gyromagnetic ratio and $|B_i|$ are the averaged internal fields on the two stopping sites. The exponential terms describe the damping of the oscillation with relaxation rates λ_1 and λ_2 and assume a Lorentzian field distribution. The amplitude A_3 and the corresponding relaxation rate λ_3 take into account a contribution of nonoscillatory signal due to the interaction of the muons with the internal fields that are parallel to the initial muon spin polarization. The best fit was achieved for the frequencies of $\nu_1 = 17.074 \pm 0.006$ MHz and $\nu_2 = 23.456 \pm 0.003$ MHz at $T = 0.2$ K, which correspond to local fields of 1.26 and 1.3 T, respectively. Furthermore, the harmonic form of the oscillations indicates that the long-range magnetic order in the ground state of $AgRuO_3$ is commensurate.

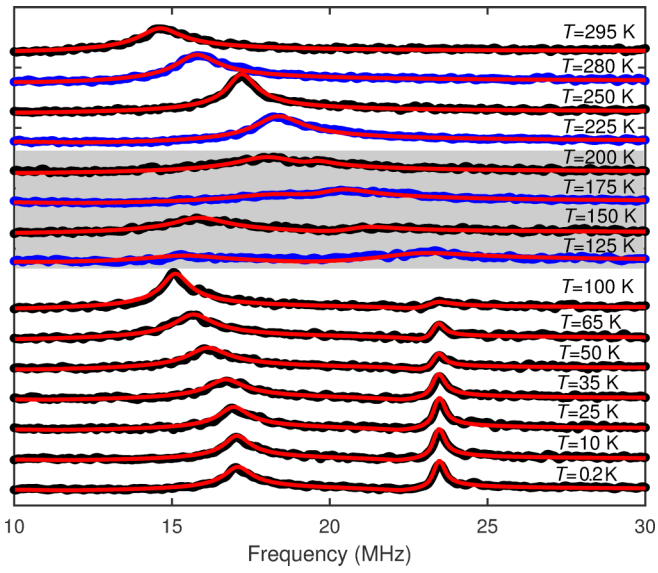

FIG. 12. Fast Fourier transformation of the muon spin precession signal measured in zero field at various temperatures using the Dolly (black) and GPS (blue) spectrometers. The FFt of the best fit to Eq. (4) is given by the red curves through the FFt data. The gray area indicates the temperature regime 125 K $\leqslant T \leqslant$ 200 K.

Further ZF-μSR measurements were performed using Dolly and GPS spectrometers to explore the temperature dependence of the harmonic modes observed at base temperature. Figure 12 shows the evolution of the FFt of ZF-μ^+SR spectra collected up to 295 K. The frequencies of the oscillations in the ZF-μ^+SR spectra correspond to the peaks in the FFt. The solid red curves represent the FFt of the best fit of the data achieved using Eq. (4). As Fig. 12 shows, there are three different temperature regimes: (i) $T < 125$ K, (ii) 125 K $\leqslant T \leqslant$ 200 K, and (iii) $T > 200$ K. Below ~125 K, there are two distinct and well-defined frequencies, the lower one noticeably softening with temperature, from ≈17 MHz at $T = 0.2$ K to ≈15 MHz at $T = 100$ K. The other one is basically T independent, at $\nu \approx 23.5$ MHz. Between $T = 125$ and 200 K the spectra are extremely broad with some traces of one or possibly two frequencies within the range $\nu \approx 16$ MHz and $\nu \approx 25$ MHz. Furthermore, the relative intensities and widths (but not frequencies!) of the spectral features in this range are very sample dependent (note that the samples used on the two different instruments were from different batches), indicating a possible role of impurities. A single sharp frequency, which is sample independent, reappears at ≈17 MHz for $T = 225$ K and is clearly visible at $T = 295$ K, at ≈15 MHz. The extracted frequencies are plotted as a function of temperature in Fig. 13. The points between 125 and 200 K, where the FFt of the signal is unclear, give our the best guesses of the possible position of two peaks in FFt, while below 125 K, two clear frequencies are observed.

Intriguingly, the enigmatic intermediate-temperature regime spans the same region where the Raman spectra undergo qualitative changes and the differential resistance is positive. It is possible that all three phenomena have the same origin. The resistance analysis and the temperature-selective μSR spectra suggest that charge dynamics related to defect traps may be relevant.

To explore the higher-temperature regime, where a single frequency was observed, ZF-μSR spectra were collected on the GPS spectrometer between 300 and 350 K with steps in temperature of 5 and 2.5 K. These data were analyzed using the function

$$A(t) = F_m[A_0 \cos(2\pi \nu_0 t) \exp(-\lambda_0 t) + A_3 \exp(-\lambda_3 t)] + (1 - F_m) G_{KT}, \quad (5)$$

where F_m is the fraction of the magnetically ordered state. This function includes a Kubo-Toyabe term G_{KT} that takes into account the contribution of the nuclear spins in the

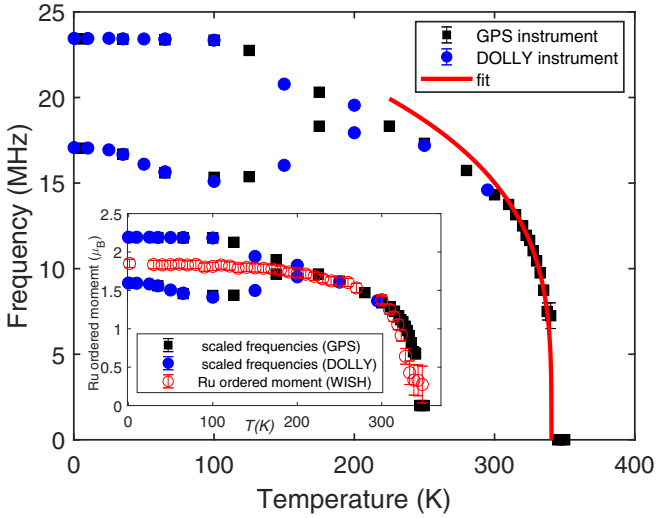

FIG. 13. Temperature dependence of the muon spin precession frequencies extracted from the analysis of ZF-μSR spectra of $AgRuO_3$. Blue circles and black squares correspond to the frequencies extracted from the muon data collected at the Dolly and GPS spectrometers, respectively. The red curve gives the best fit achieved using Eq. (6). The inset shows a comparison of the scaled ZF-μSR frequencies (blue circles and black squares) with the Ru ordered moment (red circles) from neutron diffraction data.

paramagnetic state of the electronic spin system, which was neglected at lower T. The results reveal that $T = 340$ K is the highest temperature where the oscillations exist in ZF-μ^+SR data of $AgRuO_3$. Indeed, the μ^+SR spectrum at $T = 340$ K [blue squares in Fig. 11(a)] displays a weak oscillation with frequency $\nu_0 = 7.25 \pm 0.75$ MHz extracted from the fit [corresponding red curve in Fig. 11(a)]. The FFt and fit analysis of the data at $T = 342.5$, 345, 347.5, and 350 K reveal no oscillations and are well reproduced by using only Kubo-Toyabe and nonoscillating terms. The depolarization of the asymmetry decreases progressively in the ZF-μ^+SR data at $T = 342.5$, 345, and 347.5 K, suggesting a volume-wise destruction of the magnetic state with increasing magnetic disorder. The muon polarization is fully recovered at $T = 350$ K.

The temperature dependence of the extracted frequencies (Fig. 13) can be compared with that of the Ru ordered moment from neutron diffraction because the frequencies are proportional to the local fields. The inset of Fig. 13 shows the scaled frequencies plotted over the Ru ordered moment. The curves were matched at $T = 250$ K since this temperature is far from the critical region (vicinity of T_N) where neutrons and muons have different sensitivity due to the different time scales of the techniques. The comparison reveals a generally good agreement of the temperature dependencies. The deviation above $\approx$310 K can be attributed to the fact that the ordered moment in a $k = 0$ magnetic structure may be underestimated in the vicinity of T_N, where the signal is weak.

To determine the Néel temperature T_N more accurately, and to address the issue of the critical dynamics, the temperature dependence of ν_0 was fitted by

$$\nu(t) \propto [1 - (T/T_N)]^{\beta}, \tag{6}$$

where β is the critical exponent and the range of fit was 325 K $< T <$ 337.5 K. The resulting value $T_N = 340.5 \pm 0.5$ K is

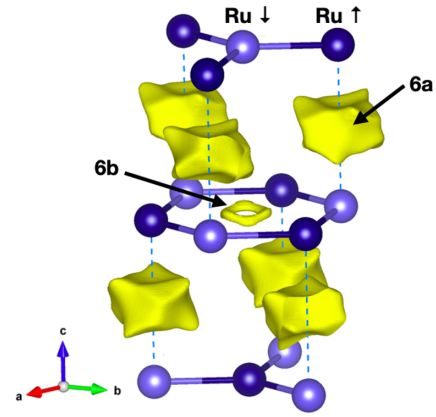

FIG. 14. Electrostatic potential in the antiferromagnetically ordered $AgRuO_3$, showing two muon-attracting regions (yellow) around the 6*b* and 6*a* sites. Each region yields six equivalent muon-trapping sites, as described in the text. The Ru atoms (purple) and some outlines of the $R\bar{3}c$ crystallographic unit cell are shown.

in excellent agreement with the Néel temperature revealed by magnetic susceptibility and other methods. However, the critical exponent $\beta = 0.27 \pm 0.02$ is considerably reduced from the conventional powers $\beta = 0.312$ [42], $\beta = 0.3485$ [43], and $\beta = 0.36$ [42] derived for the 3D Ising, 3D XY, and 3D Heisenberg magnetic systems, respectively. Such a reduction, of various strengths, can be attributed to the dominance of the two-dimensional rather than three-dimensional correlations and is often encountered in quasi-2D layered magnets (e.g., see Table A.1 in Ref. [44]). A possible explanation is the presence of long-range interactions which can affect and reduce the observed critical exponent from the theoretical predictions [45]. In particular, according to Ref. [45], $\beta = 0.27$ would correspond to a 2D magnet with a long-range interaction decaying as $\sim 1/r^{3.3}$. The presence of long-range interactions is consistent with the quasimolecular picture suggested by theory (see Sec. III G), since such orbitals typically generate long-range magnetic interactions [46].

In order to elucidate the possible nature of the observed features, we have calculated the electrostatic potential in the $R\bar{3}c$ structure (Fig. 14). The energy landscape is quite uniform, with only two minima sufficiently deep to trap muons. They are located at the 6*b* and 6*a* positions, with rhombohedral coordinates (0,0,0) and (1/4, 1/4, 1/4) at the centers of the Ru_6 hexagons and in the middle between the vertical Ru-Ru bonds, respectively. In the neutron-determined magnetic $\bar{R}3'c'$ structure, both sites have zero magnetic dipole field by symmetry. In reality, of course, the muons are shifted toward oxygens, and the calculation shows that stopping sites are $\approx$1.2 Å removed from the oxygens. For each of the two positions there are six equivalent stopping sites, corresponding to the number of surrounding oxygens. Specifically, full relaxation gives six sites around (0, 0, 0), related by trigonal symmetry, namely, shifted from (0, 0, 0) by ($\pm$0.101, 0.421, 1.10) Å, and the two others rotated by $\pm 120^\circ$, and six sites around (1/4, 1/4, 1/4), shifted by ($\pm$0.908, 0.231, 0.505) Å, and the two trigonal rotations.

At high temperature the muons might be able to hop among these six positions; if this hopping rate is of the same order as the precession frequency, the μSR signal will be greatly

broadened, and when the hopping rate becomes larger, the observed frequency will be reduced to zero, since the local field averaged over six stopping sites cancels by symmetry. Possibly, this explains our observations at 125–200 K. However, the origin of the single mode observed at higher temperature is unclear at the moment. Indeed, neutron scattering does not reveal anything unusual in terms of the long-range magnetic moment at these temperatures. Moreover, our calculations suggest that the potential barrier between (1/4, 1/4, 1/4) and (0,0,0) stopping sites is large enough to prevent muon hopping between them at these temperatures. One possibility, suggested by the transport measurements discussed above, is that defect states may play a role. If, at some characteristic temperature, defects of a particular kind (say, Ru vacancies) change their charge state, they may provide new traps for muons, thus generating a new mode. However, we do not have any direct experimental or theoretical evidence for this scenario, except that the temperature dependence of the resistivity suggests that some localized free carriers are thermally excited in this range and become itinerant. It is worth mentioning that similar frequency splitting was previously observed in other quasi-2D magnets $Sr_2CuO_2Cl_2$ [47] and $Ca_{0.86}Sr_{0.14}CuO_2$ [48] where (also) no related phase transitions were detected using neutron diffraction.

G. Electronic structure

We start with simple GGA calculations. Similar to $SrRu_2O_6$, it is only possible to achieve convergence for a Néel-AFM configuration (all nearest neighbors must be AFM ordered) [17,18]. Other solutions such as ferromagnetic (FM), zigzag AFM, or stripy AFM do not survive and collapse to the nonmagnetic configuration. This demonstrates that $AgRuO_3$ cannot be described by a conventional Heisenberg Hamiltonian, due to the itinerant nature of its electronic structure. The magnetic moment on the Ru ion is 1.24 μ_B, roughly consistent with experiment, and strongly reduced from the 3 μ_B expected for an isolated pentavalent Ru ion. Similarly to $SrRu_2O_6$, this reduction is not related to any covalency effects, but can be traced down to the formation of quasimolecular orbitals (QMOs) [17,18].

However, there is a difference between $AgRuO_3$ and $SrRu_2O_6$. First of all, in $AgRuO_3$, in the nonmagnetic state, the bands are derived from the E_{2g} and E_{1u} QMOs, rendering it metallic (see left panel in Fig. 15), while the nonmagnetic $SrRu_2O_6$ is a semiconductor with a band gap of 60 meV [17]. Accounting for the spin polarization (Néel-AFM state) opens a gap of 80 meV in $AgRuO_3$ (right panel in Fig. 15). This roughly agrees with our estimates of the fundamental gap E_g = 110–200 meV from the activated electrical resistance (see Sec. III B).

The overall band structures in $AgRuO_3$ and $SrRu_2O_6$ are similar, which again indicates the presence of QMOs [5,18] in $AgRuO_3$. However, the unit cell in $AgRuO_3$ is two times larger (different stacking along c), and therefore the number of the bands is twice that of $SrRu_2O_6$. The lowest two bands are of B_{1u} symmetry; then there are four E_{2g} bands and then six bands, two of which are of A_{1g} and four of E_{1u} symmetries.

The most important ingredient for the formation of QMOs is the oxygen-assisted hopping between unlike t_{2g} orbitals of nearest Ru ions, t_1' (if these Ru ions are in the xy plane, then these will be $xz_1 - p_z - yz_2$ and $yz_1 - p_z - xz_2$ hopping paths, where 1 and 2 are ions indices) [49]. A Wannier function projection shows that $t_1' = 0.28$ eV. There is also direct hopping between the same t_{2g} orbitals of nearest-neighbor Ru ions (for the same xy plaquette this will be hopping between xy orbitals), $t_1 = -0.27$ eV, and $t_1'/|t_1| \approx 1$. This is different from $SrRu_2O_6$, where $t_1' \approx |2t_1|$ is responsible for the formation of the QMOs [23]. Thus the QMOs are weaker in $AgRuO_3$. Antiferromagnetism works against formation of QMOs, and therefore already at this stage we expect that the intraplane exchange interaction is stronger in $AgRuO_3$.

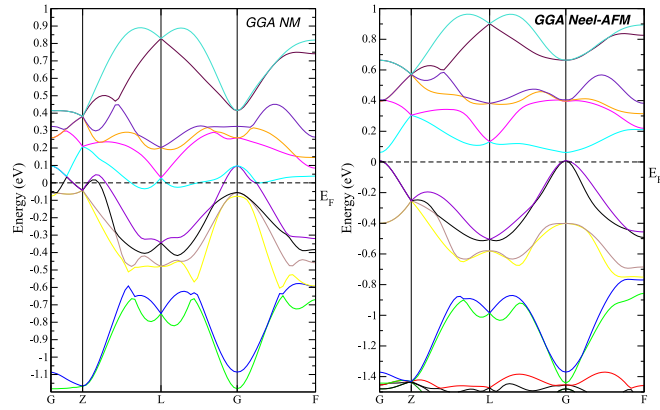

FIG. 15. Band structure as obtained in the GGA for the nonmagnetic (NM; left) and Néel-AFM (right) configurations, calculated in WIEN2K [29].

We used the total energy GGA+SOC calculations (in the Néel-AFM state) to estimate the single-ion anisotropy (SIA), which turns out to be the easy axis with $D = -12$ K, where $D = \delta E/M_z^2$, M_z is the z projection of the spin moment, and δE is the energy difference between configurations with all spins lying in and perpendicular to the Ru-Ru plane. The corresponding total energy dependence on the spin canting angle is shown in Fig. 16. We see that the SIA constant, D, in $AgRuO_3$ is slightly larger than in $SrRu_2O_6$ ($D = -9$ K) [18].

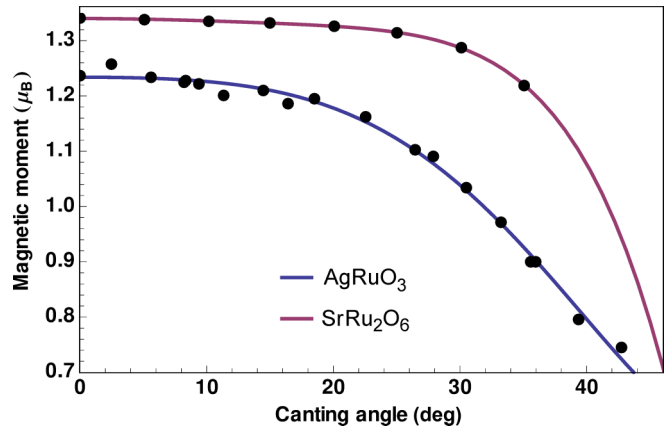

FIG. 16. Dependence of the magnetic moment on the spin canting angle ϕ. Spins of the two neighboring Ru ions are rotated in the plane of the honeycomb lattice (the angle between the spins is 2ϕ). $\phi = 0$ corresponds to the Néel-AFM structure.

The interlayer exchange interaction in $AgRuO_3$ is more tricky than in $SrRu_2O_6$ because of the different stacking. Neighboring Ru layers are shifted with respect to each other as shown in Fig. 6. As a result, there is only one shortest interplanar Ru-Ru bond (5.28 Å) for every Ru, either to a Ru atom in the plane below or to the one in the plane above. However, because of the Néel order in the planes, the net interaction between the neighboring planes is always the same for all planes and can be described by one net exchange constant. We have calculated it to be $J_\perp = 2$ K, which is much smaller than in $SrRu_2O_6$ ($J_\perp = 10$ K). The sign of the interaction is positive, which automatically ensures the AFM stacking and the $R\bar{3}'c'$ structure.

The significantly weaker interplanar coupling does not affect the magnetic properties much because it enters logarithmically as a ratio to the very large intraplane exchange coupling. Since there is a single stable magnetic configuration, one cannot recalculate J from energies of different magnetic solutions. Therefore we used the same strategy as was previously applied to $SrRu_2O_6$: We calculated in GGA+SOC the energy dependence on the spin canting angle and fitted the result to the functional presented in Ref. [18]. This yields $J =$ 96 K for Hamiltonian (3) or 255 K, if one uses magnetization instead of spins as was done in Ref. [18]. The corresponding data are shown in Fig. 16 and demonstrate that the spins are rather soft in $AgRuO_3$. If one still neglects this effect, then the spin-wave theory can be used to estimate the Néel temperature according to Refs. [50,51]. With calculated intra- and interplane exchange parameters we get $T_N = 304$ K, which is close to the experimental 342 K. Moreover, the calculated value of the intraplane exchange constant is also consistent with the Raman spectroscopy results.

IV. CONCLUSIONS

$AgRuO_3$ is a trigonal semiconducting ruthenium oxide with Ru^{5+} species in honeycomb Ru_2O_6 layers. It shows a Néel-type antiferromagnetic order below 342(3) K (335–344 K, depending on the experimental probe). The strongly anisotropic magnetic susceptibility (Fig. 1) is in agreement with the refinement of the AFM magnetic structure from the powder neutron diffraction data, as well as with first-principles calculation. The ordered Ru moments of 1.85(5) μ_B lie parallel to the c axis (magnetic point group $\bar{R}3'c'$; Fig. 6), slightly larger than the calculated moments of 1.27 μ_B, indicating a somewhat more correlated character of Ru d orbitals. Specific heat data show a second-order transition at the Néel temperature and no further transitions, in agreement with the magnetic susceptibility measurements.

The Raman and zero-field muon spin rotation (μSR) spectroscopy data indicate subtle changes occurring between 150 and 220 K. The apparent transport gap, calculated as $E_g(T) = T^2 d \ln \rho(T)/dT$, shows a negligible activation gap up to ≈40 K, which then grows up to ≈70 K, reaching ≈25 meV, and then goes down, reaching ≈0 again at $T \sim$ 160 K. After that, it grows rapidly, reaches ≈100 meV, and then remains constant up to the Néel temperature. This suggests that the intrinsic semiconducting gap is ≈100 meV, while the conductivity at low T is dominated by a small number of carriers trapped and then thermally released from some defects.

At least one Raman mode, with frequency ≈192 cm^{-1}, appears to be strongly coupled with these defects, and this coupling, as expected, is strongly temperature dependent. While all modes, including this one, are reproduced by the calculations, these calculations do not address the intensity of the Raman-allowed modes; we speculate that in the ideal crystal this mode is not visible without defect interference.

On a finer scale, one may discuss two potential energy scales. Indeed, the changes in the Raman spectra occur at $T \approx 170$ K. This temperature is roughly in the middle of the crossover region (125 K $< T <$ 200 K) identified in the ZF-μSR data, above which only a single oscillation mode is observed. Also, at about the same temperature the activation gap from electrical conductivity saturates. It is tempting to conclude that there are two energy scales, possibly associated with the two trapping sites, one of the order of 150–170 K and the other of the order of 200–225 K.

Interestingly, these defect states do not contribute to bulk properties such as the magnetic susceptibility and specific heat. The linear term in the low-T specific heat [$\gamma' = 5.6(1)$ mJ mol^{-1} K^{-2}] is sizable but not uncommonly large for a polycrystalline sample of an insulating oxide. This corroborates our picture that defects, while not changing the basic electronic structure of the compound, are responsible for the observed spectroscopic effects.

ACKNOWLEDGMENTS

We thank S. Scharsach and M. Schmidt for the DSC measurements and M. Baenitz and C. Shekhar for some measurements (not shown) in the early stage of this study. A.K.S. acknowledges the Department of Science and Technology (DST), India. S.P. received support from a DST Inspire Fellowship. I.I.M. acknowledges support from the U.S. Department of Energy through Grant No. DE-SC0021089. E.V.K. and S.V.S. thank the Russian Foundation for Basic Research (Grants No. 20-32-70019 and No. 20-32-90073) and the Russian Ministry of Science and Higher Education via program "Quantum" (Grant No. AAAA-A18-118020190095-4) and Contract No. 02.A03.21.0006. B.L. acknowledges support from the Deutsche Forschungsgemeinschaft (DFG) through Project No. B06 of the SFB 1143 (ID:247310070). This work is partially based on experiments performed at the Swiss Muon Source SμS, Paul Scherrer Institute, Villigen, Switzerland.

[1] A. Banerjee, J. Yan, J. Knolle, C. A. Bridges, M. B. Stone, M. D. Lumsden, D. G. Mandrus, D. A. Tennant, R. Moessner, and S. E. Nagler, Neutron scattering in the proximate quantum spin liquid α-$RuCl_3$, Science **356**, 1055 (2017).

[2] R. D. Johnson, S. C. Williams, A. A. Haghighirad, J. Singleton, V. Zapf, P. Manuel, I. I. Mazin, Y. Li, H. O. Jeschke, R. Valentí, and R. Coldea, Monoclinic crystal structure of α-$RuCl_3$ and the zigzag antiferromagnetic ground state, Phys. Rev. B **92**, 235119 (2015).

[3] G. M. Kanyolo, T. Masese, N. Matsubara, C.-Y. Chen, J. Rizell, Z.-D. Huang, Y. Sassa, M. Månsson, H. Senoh, and H. Matsumoto, Honeycomb layered oxides: structure, energy storage, transport, topology and relevant insights, Chem. Soc. Rev. **50**, 3990 (2021).

[4] S. A. J. Kimber, I. I. Mazin, J. Shen, H. O. Jeschke, S. V. Streltsov, D. N. Argyriou, R. Valentí, and D. I. Khomskii, Valence bond liquid phase in the honeycomb lattice material Li_2RuO_3, Phys. Rev. B **89**, 081408(R) (2014).

[5] S. V. Streltsov, Low-dimensional ruthenates with honeycomb lattice, Phys. Met. Metallogr. **119**, 1276 (2018).

[6] Z. V. Pchelkina, S. V. Streltsov, and I. I. Mazin, Spectroscopic signatures of molecular orbitals on a honeycomb lattice, Phys. Rev. B **94**, 205148 (2016).

[7] L. Šmejkal, R. González-Hernández, T. Jungwirth, and J. Sinova, Crystal time-reversal symmetry breaking and spontaneous Hall effect in collinear antiferromagnets, Sci. Adv. **6**, eaaz8809 (2020).

[8] G. Koster, L. Klein, W. Siemons, G. Rijnders, J. S. Dodge, C.-B. Eom, D. H. A. Blank, and M. R. Beasley, Structure, physical properties, and applications of $SrRuO_3$ thin films, Rev. Mod. Phys. **84**, 253 (2012).

[9] G. Cao, S. McCall, M. Shepard, J. E. Crow, and R. P. Guertin, Thermal, magnetic, and transport properties of single-crystal $Sr_{1-x}Ca_xRuO_3$ ($0 < x < 1.0$), Phys. Rev. B **56**, 321 (1997).

[10] I. I. Mazin and D. J. Singh, Electronic structure and magnetism in Ru based perovskites, Phys. Rev. B **56**, 2556 (1997).

[11] A. P. Mackenzie, A personal perspective on the unconventional superconductivity of Sr_2RuO_4, J. Supercond. Novel Magn. **33**, 177 (2020).

[12] A. Pustogow, Y. Luo, A. Chronister, Y.-S. Su, D. A. Sokolov, F. Jerzembeck, A. P. Mackenzie, C. W. Hicks, N. Kikugawa, S. Raghu, E. D. Bauer, and S. E. Brown, Constraints on the superconducting order parameter in Sr_2RuO_4 from oxygen-17 nuclear magnetic resonance, Nature (London) **574**, 72 (2019).

[13] B. E. Prasad, S. Kanungo, M. Jansen, A. C. Komarek, B. Yan, P. Manuel, and C. Felser, $AgRuO_3$, a strongly exchange-coupled honeycomb compound lacking long-range magnetic order, Chem. Eur. J. **23**, 4680 (2017).

[14] D. L. Duong, S. J. Yun, and Y. H. Lee, van der Waals layered materials: opportunities and challenges, ACS Nano **11**, 11803 (2017).

[15] C. I. Hiley, M. R. Lees, J. M. Fisher, D. Thompsett, S. Agrestini, R. I. Smith, and R. I. Walton, Ruthenium(V) oxides from low-temperature hydrothermal synthesis, Angew. Chem., Int. Ed. **53**, 4423 (2014).

[16] C. I. Hiley, D. O. Scanlon, A. A. Sokol, S. M. Woodley, A. M. Ganose, S. Sangiao, J. M. De Teresa, P. Manuel, D. D. Khalyavin, M. Walker, M. R. Lees, and R. I. Walton, Antiferromagnetism at $T > 500$ K in the layered hexagonal ruthenate $SrRu_2O_6$, Phys. Rev. B **92**, 104413 (2015).

[17] D. J. Singh, Electronic structure and the origin of the high ordering temperature in $SrRu_2O_6$, Phys. Rev. B **91**, 214420 (2015).

[18] S. Streltsov, I. I. Mazin, and K. Foyevtsova, Localized itinerant electrons and unique magnetic properties of $SrRu_2O_6$, Phys. Rev. B **92**, 134408 (2015).

[19] A. Hariki, A. Hausoel, G. Sangiovanni, and J. Kuneš, DFT+DMFT study on soft moment magnetism and covalent bonding in $SrRu_2O_6$, Phys. Rev. B **96**, 155135 (2017).

[20] S. Okamoto, M. Ochi, R. Arita, J. Yan, and N. Trivedi, Localized-itinerant dichotomy and unconventional magnetism in $SrRu_2O_6$, Sci. Rep. **7**, 11742 (2017).

[21] Y. S. Ponosov, E. V. Komleva, D. A. Zamyatin, R. I. Walton, and S. V. Streltsov, Raman spectroscopy of the low-dimensional antiferromagnet $SrRu_2O_6$ with large Néel temperature, Phys. Rev. B **99**, 085103 (2019).

[22] H. Suzuki, H. Gretarsson, H. Ishikawa, K. Ueda, Z. Yang, H. Liu, H. Kim, D. Kukusta, A. Yaresko, M. Minola, J. A. Sears, S. Francoual, H.-C. Wille, J. Nuss, H. Takagi, B. J. Kim, G. Khaliullin, H. Yava, and B. Keimer, Spin waves and spin-state transitions in a ruthenate high-temperature antiferromagnet, Nat. Mater. **18**, 563 (2019).

[23] D. Wang, W.-S. Wang, and Q.-H. Wang, t_{2g}-orbital model on a honeycomb lattice: Application to the antiferromagnet $SrRu_2O_6$, Phys. Rev. B **92**, 075112 (2015).

[24] W. Tian, C. Svoboda, M. Ochi, M. Matsuda, H. B. Cao, J.-G. Cheng, B. C. Sales, D. G. Mandrus, R. Arita, N. Trivedi, and J.-Q. Yan, High antiferromagnetic transition temperature of the honeycomb compound $SrRu_2O_6$, Phys. Rev. B **92**, 100404(R) (2015).

[25] T. Marchandier, Q. Jacquet, G. Rousse, B. Baptiste, A. M. Abakumov, and J. Tarascon, Expanding the rich crystal chemistry of ruthenium(V) oxides via the discovery of $BaRu_2O_6$, $Ba_5Ru_4O_{15}$, $Ba_2Ru_3O_{10}$, and $Sr_2Ru_3O_9(OH)$ by pH-controlled hydrothermal synthesis, Chem. Mater. **31**, 6295 (2019).

[26] T. Marchandier, G. Rousse, Q. Jacquet, A. M. Abakumov, F. Fauth, C. V. Colin, and J.-M. Tarascon, Magnetic and intercalation properties of $BaRu_2O_6$ and $SrRu_2O_6$, Chem. Mater. **32**, 8471 (2020).

[27] L. C. Chapon, P. Manuel, P. G. Radaelli, C. Benson, L. Perrott, S. Ansell, N. J. Rhodes, D. Raspino, D. Duxbury, E. Spill, and J. Norris, Wish: the new powder and single crystal magnetic diffractometer on the second, Neutron News **22**, 22 (2011).

[28] J. Rodríguez-Carvajal, Recent advances in magnetic structure determination by neutron powder diffraction, Phys. B (Amsterdam) **192**, 55 (1993).

[29] P. Blaha, K. Schwarz, G. Madsen, D. Kvasnicka, and J. Luitz, *WIEN2k, An Augmented Plane Wave + Local Orbitals Program for Calculating Crystal Properties* (Technische Universität Wien, Vienna, 2001).

[30] G. Kresse and J. Furthmüller, Efficient iterative schemes for *ab initio* total-energy calculations using a plane-wave basis set, Phys. Rev. B **54**, 11169 (1996).

[31] P. E. Blöchl, Projector augmented-wave method, Phys. Rev. B **50**, 17953 (1994).

[32] J. P. Perdew, K. Burke, and M. Ernzerhof, Generalized Gradient Approximation Made Simple, Phys. Rev. Lett. **77**, 3865 (1996).

[33] S. A. Mohitkar, W. Schnelle, C. Felser, and M. Jansen, Sr_2OsO_5 and $Sr_7Os_4O_{19}$, two structurally related, Mott insulating osmates(VI) exhibiting substantially reduced spin paramagnetic response, Inorg. Chem. **55**, 8201 (2016).

[34] N. G. Parkinson, P. D. Hatton, J. A. K. Howard, C. Ritter, F. Z. Chien, and M.-K. Wue, Crystal and magnetic structures of $A_2YRu_{1-x}Cu_xO_6$ with A = Sr, Ba and $x = 0.05$ to 0.15, J. Mater. Chem. **13**, 1468 (2003).

[35] H. T. Stokes, D. M. Hatch, and B. J. Campbell, ISOTROPY Software Suite, 2019, http://iso.byu.edu.

[36] B. J. Campbell, H. T. Stokes, D. E. Tanner, and D. M. Hatch, ISODISPLACE: a web-based tool for exploring structural distortions, J. Appl. Crystallogr. **39**, 607 (2006).

[37] See Supplemental Material at http://link.aps.org/supplemental/10.1103/PhysRevB.103.214413 for a table and three additional figures with Raman spectroscopy data.

[38] P. G. Klemens, Anharmonic decay of optical phonons, Phys. Rev. **148**, 845 (1966).

[39] P. Knoll, C. Thomsen, M. Cardona, and P. Murugaraj, Temperature-dependent lifetime of spin excitations in $R\mathrm{Ba_2Cu_3O_6}$ (R = Eu, Y), Phys. Rev. B **42**, 4842 (1990).

[40] H. Gretarsson, N. H. Sung, M. Höppner, B. J. Kim, B. Keimer, and M. Le Tacon, Two-Magnon Raman Scattering and Pseudospin-Lattice Interactions in $\mathrm{Sr_2IrO_4}$ and $\mathrm{Sr_3Ir_2O_7}$, Phys. Rev. Lett. **116**, 136401 (2016).

[41] A. Suter and B. Wojek, Musrfit: A free platform-independent framework for μSR data analysis, Phys. Procedia **30**, 69 (2012).

[42] S. T. Bramwell, P. Day, M. T. Hutchings, J. R. G. Thorne, and D. Visser, Neutron scattering and optical study of the magnetic properties of the two-dimensional ionic ferromagnets $\mathrm{Rb_2CrCl_3Br}$ and $\mathrm{Rb_2CrCl_2Br_2}$, Inorg. Chem. **25**, 417 (1996).

[43] M. Campostrini, M. Hasenbusch, A. Pelissetto, P. Rossi, and E. Vicari, Critical behavior of the three-dimensional XY universality class, Phys. Rev. B **63**, 214503 (2001).

[44] A. Taroni, S. T. Bramwell, and P. C. W. Holdsworth, Universal window for two-dimensional critical exponents, J. Phys.: Condens. Matter **20**, 275233 (2008).

[45] M. E. Fisher, S. K. Ma, and B. G. Nickel, Critical Exponents for Long-Range Interactions, Phys. Rev. Lett. **29**, 917 (1972).

[46] S. M. Winter, A. A. Tsirlin, M. Daghofer, J. van den Brink, Y. Singh, P. Gegenwart, and R. Valentí, Models and materials for generalized Kitaev magnetism, J. Phys.: Condens. Matter **29**, 493002 (2017).

[47] L. P. Le, G. M. Luke, B. J. Sternlieb, Y. J. Uemura, J. H. Brewer, T. M. Riseman, D. C. Johnston, and L. L. Miller, Muon-spin-rotation studies in single-crystal $\mathrm{Sr_2CuO_2Cl_2}$, Phys. Rev. B **42**, 2182 (1990).

[48] A. Keren, L. P. Le, G. M. Luke, B. J. Sternlieb, W. D. Wu, Y. J. Uemura, S. Tajima, and S. Uchida, Muon-spin-rotation measurements in infinite-layer and infinite-chain cuprate antiferromagnets: $\mathrm{Ca_{0.86}Sr_{0.14}CuO_2}$ and $\mathrm{Sr_2CuO_3}$, Phys. Rev. B **48**, 12926 (1993).

[49] I. I. Mazin, H. O. Jeschke, K. Foyevtsova, R. Valentí, and D. I. Khomskii, $\mathrm{Na_2IrO_3}$ as a Molecular Orbital Crystal, Phys. Rev. Lett. **109**, 197201 (2012).

[50] B. Schmidt, M. Siahatgar, and P. Thalmeier, Stabilization of Néel order in frustrated magnets with increasing magnetic field, EPJ Web Conf. **40**, 04001 (2013).

[51] E. V. Komleva, V. Yu. Irkhin, I. V. Solovyev, M. I. Katsnelson, and S. V. Streltsov, Unconventional magnetism and electronic state in the frustrated layered system $\mathrm{PdCrO_2}$, Phys. Rev. B **102**, 174438 (2020).